The Astrophysical Journal, 793:86 (11pp), 2014 October 1 doi:10.1088/0004-637X/793/2/86



# BIRTH, LIFE, AND DEATH OF A SOLAR CORONAL PLUME

Stefano Pucci[1], Giannina Poletto[2], Alphonse C. Sterling[3], and Marco Romoli[1]
[1] Department of Physics and Astronomy, University of Firenze, Largo Enrico Fermi 5, I-50125 Firenze, Italy; stpucci@arcetri.astro.it
[2] INAF-Arcetri Astrophysical Observatory, Largo Enrico Fermi 5, I-50125 Firenze, Italy
[3] Space Science Office, NASA/MSFC, Huntsville, AL 35812, USA
*Received 2014 June 5; accepted 2014 August 1; published 2014 September 10*

## ABSTRACT

We analyze a solar polar-coronal-hole (CH) plume over its entire ≈40 hr lifetime, using high-resolution *Solar Dynamic Observatory* Atmospheric Imaging Assembly (AIA) data. We examine (1) the plume's relationship to a bright point (BP) that persists at its base, (2) plume outflows and their possible contribution to the solar wind mass supply, and (3) the physical properties of the plume. We find that the plume started ≈2 hr after the BP first appeared and became undetectable ≈1 hr after the BP disappeared. We detected radially moving radiance variations from both the plume and from interplume regions, corresponding to apparent outflow speeds ranging over ≈(30–300) km $s^{-1}$ with outflow velocities being higher in the "cooler" AIA 171 Å channel than in the "hotter" 193 Å and 211 Å channels, which is inconsistent with wave motions; therefore, we conclude that the observed radiance variations represent material outflows. If they persist into the heliosphere and plumes cover ≈10% of a typical CH area, these flows could account for ≈50% of the solar wind mass. From a differential emission measure analysis of the AIA images, we find that the average electron temperature of the plume remained approximately constant over its lifetime, at $T_e \approx 8.5 \times 10^5$ K. Its density, however, decreased with the age of the plume, being about a factor of three lower when the plume faded compared to when it was born. We conclude that the plume died due to a density reduction rather than to a temperature decrease.

*Key words:* Sun: activity – Sun: corona – Sun: UV radiation – techniques: spectroscopic

*Online-only material:* color figures

## 1. INTRODUCTION

Solar plumes are most visible when they exist in polar regions: indeed, they have long been observed at times of eclipses, when they trace the open field lines rooted in the unipolar magnetic field of polar coronal holes (CHs). The advent of space instrumentation enormously extended our capabilities for observing plumes and provided us with a large amount of previously unavailable data about their behavior in UV radiation. These objects are interesting not only per se, but also because their role in solar wind remains controversial (e.g., do they supply wind mass?). It is also uncertain whether they can be identified in the solar wind (e.g., how far do they maintain their identity in the extended corona?).

Before we can answer these questions, we need to have a better knowledge of the behavior of plumes; their generation, disappearance, lifetime, and the temporal evolution of their physical parameters, are, as of today, not fully defined. In this work, we focus on a single plume, one that we follow from birth to death over its nearly two-day lifetime. We aim at measuring the plume's temperature, density, and outflow speed (if any) and at analyzing the evolution with time of these quantities; such time variations have not yet been discussed.

Our analysis is based on observations made by the Atmospheric Imaging Assembly (AIA; Lemen et al. 2012) on board the *Solar Dynamic Observatory* (*SDO*; Pesnell et al. 2012), over 2010 August 28 and 29. The plume is rooted in the northern CH, close to the pole of the Sun, and is visible in most AIA channels, though at differing phases of its life and with differing contrast with respect to the background corona. It originates in a bright point (BP), whose radiance changes with time. In the past, many plume–BP combinations have been observed (see, e.g., Del Zanna et al. 2003; Wang & Muglach 2008); we provide further information on this issue by describing the relationship between our plume and its associated BP.

CHs are known to be sources of high speed wind, and, with plumes being the densest regions within CHs, a seemingly reasonable assumption is that they are sources of (most of) the wind mass. In the past, authors obtained conflicting results on this issue, with some claiming that plumes are quasi-static, and others claiming that they may contribute significantly to the solar wind (see Table 2 of Wilhelm et al. 2011, for a compendium of different results). Most of these studies adopted the Doppler dimming technique to obtain the speed of plasma in the intermediate corona, while the most recent investigations focused on revealing the occurrence of outflows in plumes at lower heights in the corona (McIntosh et al. 2010; Krishna Prasad et al. 2011; Tian et al. 2011), by using space–time plots of UV radiance from data acquired by the *Solar Terrestrial Relation Observatory* (*STEREO*) and *SDO* experiments. Here, we used AIA data to build space–time plots in different AIA channels and check whether the outflow speed of the propagating disturbances is a function of temperature. We also built space–time plots at a few times during the plume lifetime, looking for time evolution of the observed upflowing events as the plume fades.

Several authors inferred the electron temperature ($T_e$) and density ($n_e$) of plumes from either emission measure (EM), differential emission measure (DEM), or line ratio analyses. It turns out that $T_e$ and $n_e$ in plumes are, respectively, slightly lower and higher than their values in the ambient corona (see Tables 3 and 4 of Wilhelm et al. 2011, for a summary of past results). A few authors have also given the profile of $T_e$ and $n_e$ versus heliocentric distance over a limited range of altitudes. However, no information is available about the behavior of these quantities over the plume lifetime. Because AIA observations

in multiple spectral bands are available, here we adopt a DEM technique that allows us to follow the changes of the physical parameters of the plume material as it evolves over time. As we describe in Section 4, the plume turns out not to be strictly isothermal, and it is its density rather than its temperature that decreases as the plume decays.

In Section 2, we describe the data set that we analyze and the BP–plume relationship; Sections 3 and 4 illustrate, as functions of time, the behavior, respectively, of the outflow speed and of the electron temperature and density of the plume; and, in Section 5, we summarize our results and give a crude estimate of the mass that plumes possibly provided to the solar wind.

## 2. THE DATA AND THE BP-PLUME RELATIONSHIP

The data that we analyze were acquired by the *SDO* AIA experiment over two days, from 00 UTC on August 28, to 24 UTC on 2010 August 29. AIA takes full-disk images of the Sun, with a time cadence of 12 s, in 10 UV and EUV wavelengths, with a plate scale of 0.″6 per pixel. In the following, we use data acquired in the 94 Å, 131 Å, 171 Å, 193 Å, 211 Å, 193 Å, 304 Å, and 335 Å EUV channels.

We chose a region near the solar north pole within a small CH, where BPs and plumes are rooted. Although stable in size, the CH covers a small area north of the 70° latitude. The adjacent quiet sun emission may extend to high altitudes and appear as a diffuse haziness beyond the limb of the Sun. This has little effect on the plume analysis (because, as described in Section 4, for each image, we subtract the ambient background component from the total observed emission), but may lead to an overestimation of the temperature or density of the interplume background. Figure 1 gives images of the BP and plume, obtained by summing data over a 10 minute accumulation time, in the 171 Å, 193 Å, and 211 Å channels, on August 28, from 08:40 to 08:50 UTC and from 19:58 to 20:08 UTC (respectively, top and middle row) and on August 29, from 06:00 to 06:10 UTC (bottom row), with an exposure time of 100 s in the 171 Å channel, and of 145 s in the other channels.

The dashed and dotted lines in the A panel give the position and size of the horizontal "slits" adopted to evaluate the evolution in space and time of the BP and the plume that appear in Figures 2 and 3. The dashed boxes in the D panel give the position and size of the vertical "slits" adopted to build the space–time plots, given in Figures 4–6. The dashed box in the G panel gives the position and size of the vertical "slit" adopted to build the space–time plot, given in Figure 7.

In CH regions, we expect (O'Dwyer et al. 2010) the 171 Å channel to be dominated by the Fe IX 171.07 Å line (with a temperature of maximum ion abundance $T_e = 0.7 \times 10^6$ K), while the 193 Å channel maximum response is over $0.7 \times 10^6$ K $\leqslant T_e \leqslant 1.6 \times 10^6$ K. The 211 Å channel emission arises from Fe X and Fe XI lines, with maximum response at, respectively, $T_e = 1.1 \times 10^6$ K and $T_e = 1.4 \times 10^6$ K (and add to Cr IX emission, with a maximum response at $T_e = 0.9 \times 10^6$ K). Hence, in Figure 1 the 193 Å and 211 Å images show hotter plasma than that imaged by the 171 Å channel. Figure 1 reveals that the plume plasma is cooler than the ambient corona, while loops bridging over bipoles forming the BP at the base of the plume are hotter than the plume.

The evolution of the plume and the BP over their entire lifetimes is shown, respectively, in the left (plume) and right (BP) panels of Figure 2. These profiles have been constructed by examining plasma within virtual horizontal slits (dashed parallel lines in panel A of Figure 1), that cut through the BP and/or the plume, and plotting the 171 Å channel radiance within the slit at different times. We used data accumulated over an altitude interval of 6″ for the BP and of 30″ for the plume, with a cadence of 120 s. Clearly both features are carried around the Sun by solar rotation, and the resulting longitudinal shift agrees with values given by Gupta et al. (2012) for the rotation rate at high latitudes. The west–east shift of the BP–plume complex reveals that the plume is rooted on the far side of the Sun: hence, we do not know whether we see the whole, or only a fraction, of the BP total area.

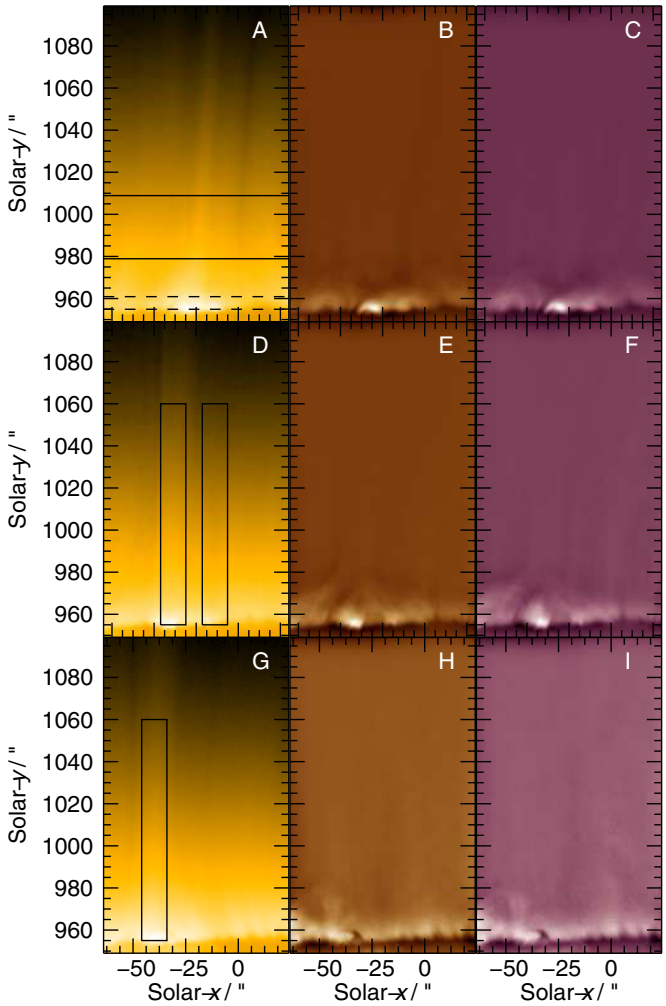


**Figure 1.** Images of the BP–plume complex, in the 171 Å (left panels), 193 Å (middle panels), and 211 Å (right panels) AIA channels, from data accumulated over 10 minutes, i.e., 50 images for each panel. Top row (A, B, and C panels) shows data from the early phase of the plume (08:40 UTC, on August 28), while middle and bottom rows show, respectively, data from the peak phase (19:58 UTC on August 28) and decaying phase (06:00 UTC on August 29). We adopted a logarithmic scale for the colors in the 171 Å panels, to enhance the visibility of the plume at high altitudes. An unsharp mask has been used in the 193 Å and 211 Å filter images for a better display of the loops at the base of the plume. For further details see the text.

(A color version of this figure is available in the online journal.)

The right panel of Figure 2 suggests that the BP first appears at ≈02:00 UTC on August 28 and its radiance maximizes at ≈8:30 UTC. It steadily decreases afterward, until it dies a little before 12 UTC on August 29. The plume first appears at ≈04:00 UTC on August 28, and blends with the background from ≈12 UTC onward on August 28. Hence, there is no plume before the BP emergence, but the plume survives the BP, though for a short time.

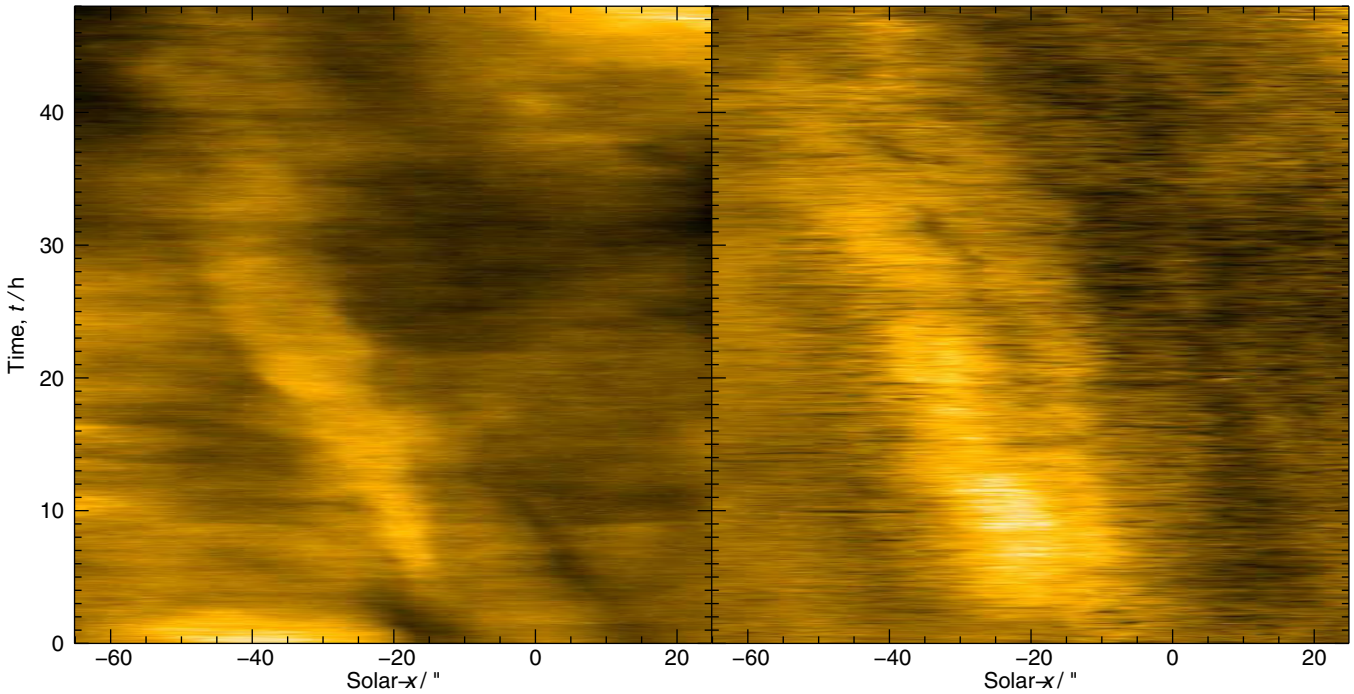


**Figure 2.** Left panel: radiance in the AIA 171 Å channel at the location of the plume, shown against time and solar $x$. Data in this plot were accumulated over an altitude interval of 30″ (between the two upper short-dashed lines in panel A of Figure 1), and sampled every 120 s, over a time interval from 00:00 UTC on August 28, to 00:00 UTC on August 30. Right panel: radiance in the AIA 171 Å channel at the location of the BP where the plume is rooted, shown against time ($y$ axis) and position ($x$ axis). Data in this plot were accumulated over an altitude interval of 6″ (between the two lower long-dashed lines in panel A of Figure 1), and sampled every 120 s, over a time interval from 00:00 UTC on August 28, to 00:00 UTC on August 30.

(A color version of this figure is available in the online journal.)

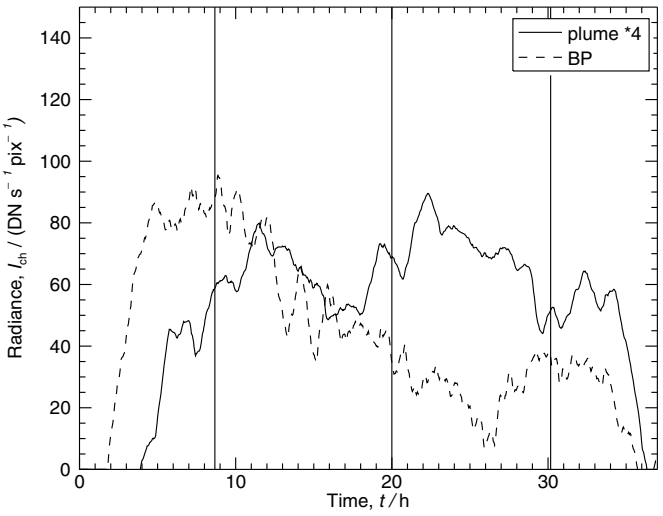


**Figure 3.** Background-removed radiance of the BP (dashed line) and of the plume (solid line) in the 171 Å channel, measured every 120 s over the whole lifetime of the BP–plume complex. (The plume radiances are multiplied by a factor of four for clarity.) The plume and BP regions were defined in the same way as in Figure 2 (i.e., using the upper- and lower-pair of dashed lines in Figure 1(A)). Vertical lines give the times when plume data have been analyzed. See the text for details.

We also examined the 304 Å channel data, looking for jets that might occur before the birth of the plume: usually this channel samples a relatively cold chromospheric plasma. Indeed, a blowout jet lasting from 01:35 to 02:00 UTC is clearly visible in the 304 Å data, and, though briefly and less conspicuously, in the 171 Å channel. Hence, ≈2 h before the plume shows up, a precursor jet occurs, consistent with the Raouafi et al. (2008) results. At later times, however, we no longer used the 304 Å channel, since, for this study, we chose to focus on the hotter plume emissions.

A more direct view of the BP–plume relationship than that given by Figure 2 is shown in Figure 3 where we give the background-subtracted radiances of the BP and the plume, in the 171 Å channel, over the lifetime of both features. The figure has been constructed from data taken every 2 minutes and smoothed with a running average boxcar of 40 minutes. As in Figure 2, data for the BP have been accumulated over the height interval between solar-$y = 955''$and solar-$y = 961''$ (i.e., 10 pixels), while plume data have been accumulated over the height interval between solar-$y = 979''$ and solar-$y = 1009''$ (50 pixels). At any time, the horizontal "box" is centered at the same position for both structures and keeps a constant size, though shifting in time to follow the eastward-moving solar rotation of both structures.

Over its lifetime, the BP shows brightenings and/or weakenings. The plume radiance, however, fluctuates less than the BP radiance; although initially brightening as the BP brightens, at later times the plume appears to be little affected by the BP's changes. Thus, for this case, it appears as if the BP is a prerequisite for the formation (and persistence) of the plume. However, at later times the plume is apparently not sensitive to phenomena that modify the BP, other than dying shortly after the BP fades.

Radiance oscillations in BPs have been detected by many authors (see, e.g., Kariyappa and Varghese 2008; Chandrasekhar et al. 2013) who claim that they occur over a large variety of timescales (from minutes to hours) and are possibly periodic (with periods of the order ranging from 10 to 25 minutes). It is beyond the scope of this work to investigate the nature of the fluctuations here, nor, on the basis of this single case, can we draw any conclusions on the general BP–plume relationship. However, relative brightenings (of the order of 3% of the

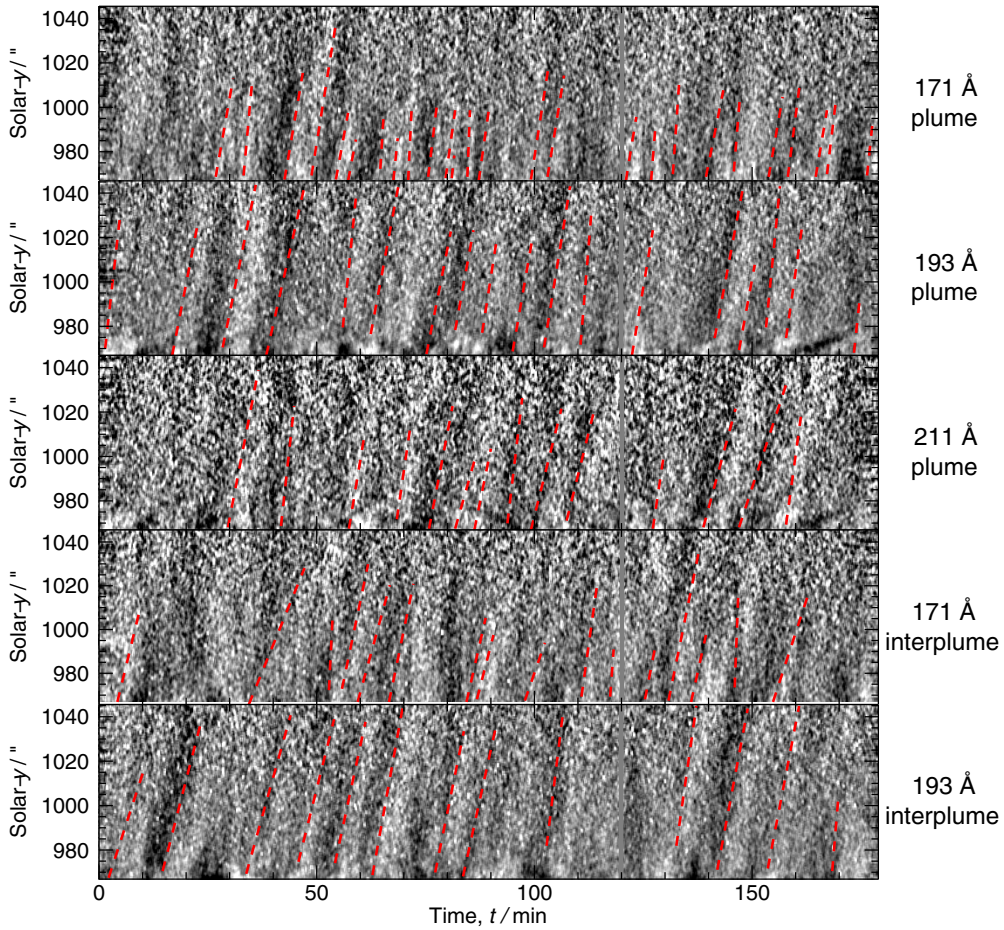


**Figure 4.** Space–time plot of the detrended radiances of the plume in the 171 Å, 193 Å, and 211 Å channels (topmost three panels), over the time interval from 19:00 to 22:00 UTC on 2010 August 28. The ordinate gives the solar $y/''$ and the abscissa gives time ($t$/min) after 19:00 UTC, on 2010 August 28. Plume data have been accumulated over the left vertical virtual slit shown in panel D of Figure 1. Bottom two panels: same as the top two panels, in the background interplume corona. Background data have been accumulated over the right vertical virtual slit shown in panel D of Figure 1. The white dashed lines (red in the color online version) have been added to help the reader trace upflowing events. The boxcar used in the detrending procedure is 75 images (15 minutes) wide; see the text for further details.
(A color version of this figure is available in the online journal.)

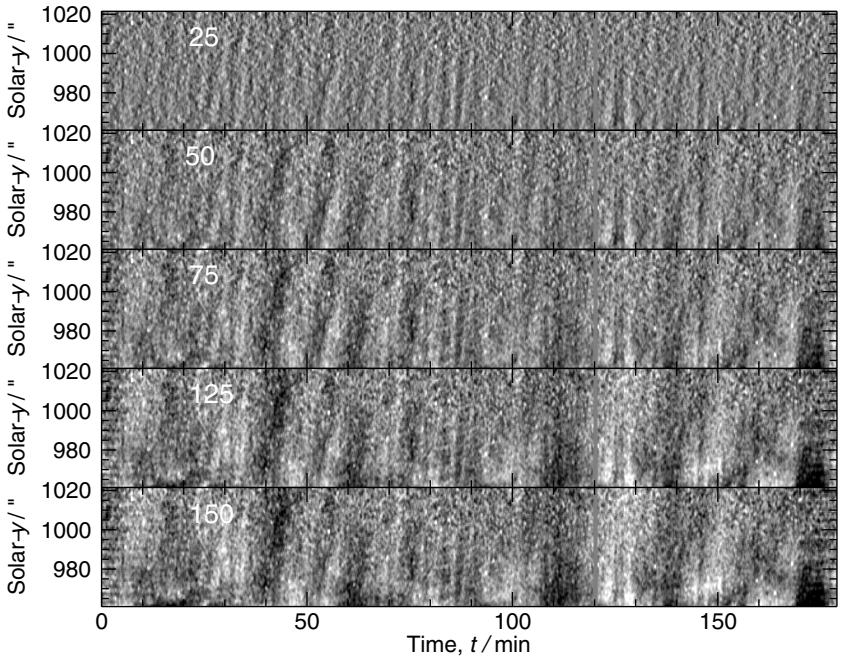


**Figure 5.** Space–time plot of the detrended radiance of the plume in the 171 Å AIA channel, over the same time interval used in Figure 4 on 2010 August 28, when the plume was brightest. Otherwise, the same as the upper panel of Figure 4, except that the detrending procedure has been done using boxcars of widths span times ranging from five minutes (top panel) to 30 minutes (bottom panel, i.e., from 25 to 150 images).

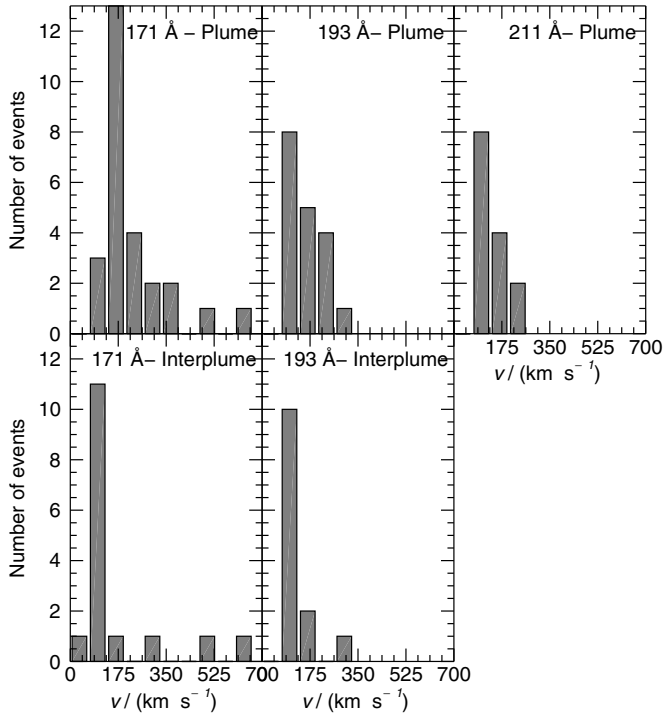


**Figure 6.** Histograms showing outflow-speed ($v$/km s$^{-1}$) distributions of outflowing events in the plume (top row) and interplume background (bottom row) corona, in the 171 Å, 193 Å, and 211 Å AIA channels for the plume, and in the 171 Å and 193 Å channels for the interplume background corona, on 2010 August 28, inferred from the data shown in Figure 4. Boxcar width: 75 images.

time-averaged local plume emission) are characteristic aspects of plumes. Hence, we conclude that, in this case, the occurrence of a BP seems to be necessary to create the conditions for the plume to develop, but the process leading to the BP is not the only factor that fuels the plume, because plume fluctuations are small compared to BP fluctuations. Indeed, as suggested by Zhang et al. (2012), only the strongest BP flashes, which we do not observe, may be associated with jets and cause plume brightenings.

## 3. OUTFLOWS IN PLUMES

Outflows in plumes have been studied by a few authors (see, e.g., Gabriel et al. 2003; Teriaca et al. 2003) via the Doppler Dimming technique (Noci et al. 1987), applied to observations made by the UltraViolet Coronograph and Spectrometer on board the *Solar and Heliospheric Observatory* (*SOHO*) at altitudes of the order of 1.4–2.4 solar radii. At lower altitudes, data acquired in CHs by the *SOHO* Solar Ultraviolet Measurement of Emitted Radiation (SUMER) and/or the *Hinode* EUV Imaging Spectrometer (EIS) have been analyzed for spectroscopic signatures of upflows (see, e.g., Wilhelm et al. 2000; Tian et al. 2010); these works provide information on the sites where the solar wind originates, but add little information to its outflow speed profile. At altitudes ranging from 100″ to 150″ above the limb of the Sun, several authors (McIntosh et al. 2010; Tian et al. 2011; Krishna Prasad et al. 2011; Gupta et al. 2012) adopted a different technique to analyze data, using space–time plots of propagating outflows. Although upflow signatures have been detected both in plumes and in interplume ambient plasma, the nature of these signatures is still debated, as it is not clear whether they are due to waves or whether they represent outflowing material (McIntosh et al. 2010). McIntosh et al. (2010), for instance, from data taken by the Extreme Ultraviolet Imaging package on board *STEREO*, suggested that high-speed outflowing jets, with a mean speed of the order of 135 km s$^{-1}$, might repeatedly occur in plumes. These authors built a time series of

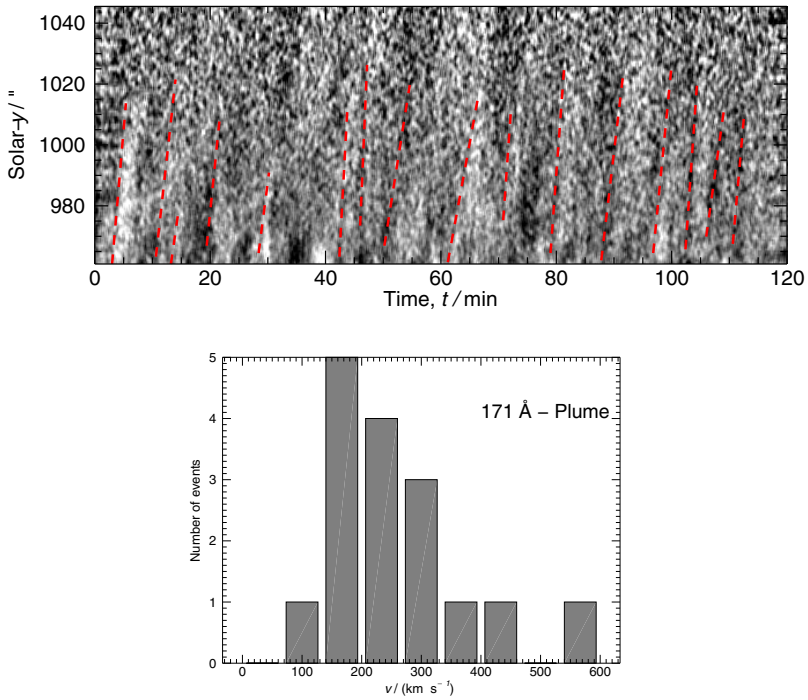


**Figure 7.** Top panel: space–time plot of the detrended 171 Å radiance of the plume region on 2010 August 29, in the 171 Å over the 2 h time interval 05:00 UTC–07:00 UTC; this time period is during the final stage of the plume's life. Boxcar width used was 75 images. White dashed lines (red in the color online version) trace upflowing events. Bottom panel: histogram showing the upflow speed distribution of outflowing events, over the same time interval as the upper panel.

(A color version of this figure is available in the online journal.)

detrended images, along a virtual slit set normal to the limb of the Sun. We adopt the same technique to analyze our data.

Figure 4 shows space–time plots of the plume radiance in the 171 Å, 193 Å, and 211 Å AIA channels (top three panels) and of the interplume radiance in the 171 Å and 193 Å AIA channels (bottom two panels), over three hours, from 19:00 to 22:00 UTC on August 28. The panels cover an altitude interval of 80″; the bottom level has been set to a solar-$y = 965''$. The width of the virtual slit is 12″ (20 pixels) and is centered, in the plume case, at solar-$x = -31''$ and, for the ambient background corona at solar-$x = -11''$. Figure 4 displays "detrended" residual radiances as functions of time, following the procedure of Tian et al. (2011): after forming initial space–time plots over the virtual slits, we subtracted off 15 minutes (i.e., 75 images) running boxcar averages from the initial space–time plots, and then we normalized to the running average. Compared to the initial space–time plots, these detrended space–time plots improve the visibility of fainter moving features. We do not show the space–time plot of the background corona in the 211 Å AIA channel, because it is too noisy (the 211 Å channel has a lower signal-to-noise ratio than the 171 Å and 193 Å channels).

The result in Figure 4 shows alternating oblique dark and bright strips that extend upward over time; these represent plasma flows, and the larger the inclination of the strip with respect to the time (horizontal) axis, the higher the speed. The relative radiance fluctuations are low level, being of the order of a few percent. Many flows are apparent over the plotted timespan; all of these flows are from the slit regions, but our spatial resolution in the $x$ direction is dictated by the 12″ width of the virtual slit. To help the reader visualize the upflowing events and, at least qualitatively, their speed, dashed lines have been overplotted onto propagating disturbances. These lines trace the position of the highest radiance gradient: for "thin" (in the time dimension) outflows, the line overlays the event; for "wide" outflows, the line has been drawn to the left of the event. Clearly, both the plume and interplume panels host a variety of different outflow speeds.

Before discussing the results of Figure 4, we check whether the choice of the width of the boxcar in the detrending procedure affects the visibility of the events. Figure 5 shows the space–time plots of the AIA 171 Å radiance, over the same time interval used in Figure 4, built from boxcar widths ranging from 25 to 150 images, i.e., from 5 to 30 minutes. It turns out that long duration events, such as that occurring at $t = (42–50)$ minutes, may go unnoticed when narrow boxcars are adopted; this is because the wider the boxcar, the greater the radiance of long events. On the contrary, the isolated, thinnest (briefest) events, such as that at $t = 80$ minutes, when wider boxcars are used, tend to blend within the wide "events" that show up when large-size boxcars are adopted. We conclude that outflowing episodes can be detected independent of the width of the boxcar, though the longest events are better identified with wider boxcars and short duration outflows are more easily spotted with narrower boxcars.

Going back to Figure 4, we point out that, in the 171 Å channel, the plume hosts a larger number of events (26) than the background interplume ambient corona (16). The speed distributions of the upflows are shown in Figure 6, both for the plume (top row) and for the background (bottom row). The histograms have a bin size of 66 km s$^{-1}$: in the 171 Å channel, the plume distribution peaks at $v \approx 167$ km s$^{-1}$, with a median value of 185 km s$^{-1}$, while in the interplume ambient corona the distribution peaks at $v \approx 100$ km s$^{-1}$, with a median value of 110 km s$^{-1}$. Hence, the plume upflowing disturbances are more numerous and have higher speeds than disturbances in the ambient corona.

Figure 7 gives the space–time distribution over a two hour interval (05:00–07:00) UTC on August 29 at a time close to the final stage of the plume. Alternating bright/dark strips are still visible, with an upflow speed possibly even higher than that observed at earlier times; the distribution of upflowing events peaks at $v \approx 167$ km s$^{-1}$, but the median value is now ≈258 km s$^{-1}$. The event rate, however, is about the same as we detected during the earlier time period, being 8/hr here compared to 8.7/hr in the initial stage of the plume's life in Figure 6. We conclude that the time series analysis of images taken at different stages in the plume's evolution reveals that the upflowing disturbances are seen throughout the plume lifetime, without major changes, either in their frequency of occurrence or in the peak of their outflow propagation speed distributions.

We now examine whether the occurrence of outflows depends on temperature, i.e., on their observation in different AIA channels. To this end, we compare space–time plots in the 171 Å, 193 Å, and 211 Å AIA channels. Figure 4 shows that outflows occur in all channels, though not necessarily at the same time, nor with the same width (i.e., time duration). For instance, the 171 Å upflow at $t = 50$ minutes is missing in the 193 Å channel emission. On the other hand, a 193 Å upflow at $t = 110$ minutes is missing in the 171 Å channel. The altitude reached by the bright strips before becoming too noisy to be identified is not relevant for our current investigations, because the apparent fading of the trajectories may depend on instrumental factors rather than on the physics of the events.

The middle and right panels of Figure 6 give the distribution of the outflow speed in the 193 Å and 211 Å AIA channels. It turns out that the peak and median values of the 171 Å disturbances ($v \approx 167$ km s$^{-1}$ and 185 km s$^{-1}$) are higher than those from the 193 Å and 211 Å channel distributions. The latter share the same value of the peak ($v \approx 100$ km s$^{-1}$), and the median value of the two distributions is quite similar (143 km s$^{-1}$ and 124 km s$^{-1}$, respectively, for the 193 Å and 211 Å channel). Often, the speed of outflowing events has been compared with the sound speed, $C_s/(\mathrm{ms}^{-1}) = 152(T_e/\mathrm{K})^{1/2}$ (Priest 1984), to ascertain whether the observed disturbances might be interpreted in terms of slow magnetosonic waves propagating upward. In this case, we expect a temperature dependence of the outflow speed that is not observed in our data, as disturbances in the 171 Å channel propagate at a higher speed than disturbances in the "hotter" 193 Å and 211 Å channels. We will come back to this issue in Section 5.

## 4. ELECTRON DENSITY AND TEMPERATURE IN PLUMES

If plumes were strictly isothermal, the ratio of the emission in two different AIA channels would give their temperature, provided that the plasma sampled by the two AIA filters originates from the same regions and that ionization equilibrium holds. In that case, the measured radiances, $I_{ch}$ (data number per second per pixel), depend on the filter responses, $F_{ch}$, which in turn are a function of temperature, $T_e$ (and also on the elemental abundances), as shown by the following relationship:

$$I_{ch} = \int F_{ch}(T_e) n_e^2 \mathrm{d}l, \quad (1)$$

where $n_e$ is the plasma density and the integral extends along the line-of-sight (LOS) path. The capability of using data from

many AIA channels leads to a more precise evaluation of $T_e$, as all the ratios should converge to a unique temperature value. However, taking into consideration the results from Section 3, where we found evidence for the occurrence of upflows of differing temperatures, we are lead to dismiss the hypothesis of isothermal plumes. Therefore, instead of the above isothermal-assumption formulation, we will use a different technique to evaluate the electron temperature and density.

To this end, we rewrite Equation (1) in a slightly different way,

$$I_{ch} = \int F_{ch}\epsilon(T_e)dT_e, \quad (2)$$

where $\int \epsilon(T_e)dT_e = \int n_e^2 dl$ and $\epsilon(T_e) = (n_e^2 dl/dT_e)$ is the DEM. This alternative formulation allows us to evaluate the amount of plasma at different temperatures within the plume. There are several algorithms to infer the $\epsilon(T_e)$ as a function of $T_e$ distribution from observed radiances; here, we adopt the technique recently developed by Plowman et al. (2013) that allows a fast reconstruction of $\epsilon(T_e)$ distributions and has been tested on AIA (and EIS) data. We refer the reader to Plowman et al. (2013) for details on their method. The AIA $F_{ch}$ functions have been determined by combining the wavelength-dependent instrumental response with the emissivity model given by the CHIANTI 7.1 version, with the empirical corrections to the 94 and 131 Å channels suggested by Boerner et al. (2014).

In order to evaluate the physical parameters of plumes, we have to take into account that plumes are embedded in an ambient medium, the background corona; this background is multi-thermal as well, and often only slightly fainter than the plumes. The residual emission of the plume, which in principle can be determined by subtracting the background emission from the LOS-integrated radiance, is hard to determine in practice. This is especially true when, for example, the background radiance changes across the width of the plume, or when using data from channels where the emission of the plumes is only marginally higher than that of the background. Hence, in order to deal with count rates high enough to minimize the statistical uncertainty of the data used in the $\epsilon(T_e)$ calculation, we chose instead to work with the integrated plume+background radiance at the plume location, and to evaluate the background emission at positions devoid of plumes.

Figure 8 shows the $\epsilon(T_e)$ versus $T_e$ profiles of the LOS-integrated emission, at a solar-$y = 1003''$ along the axis of the plume (solid line), and at a position devoid of plumes (dotted line). The difference between these two curves therefore represents the $\epsilon(T_e)$ versus $T_e$ profile of the plume itself. Here, the original data, acquired on 2010 August 28, have been integrated over the 10 minute interval from 19:58 to 20:58 UTC, when the plume reached its peak radiance. The figure shows that the $\epsilon(T_e)$ of the plume+background is slightly higher than the background $\epsilon(T_e)$ in the regime $0.7 \times 10^6$ K $\leqslant T_e \leqslant 1.1 \times 10^6$ K, but above $T_e = 1.1 \times 10^6$ K all of the emission originates in the background. Integrating over temperature, we obtain an EM of the plume+background of $3.0 \times 10^{26}$ cm$^{-5}$, which is higher by only 10% over the background EM of $2.7 \times 10^{26}$ cm$^{-5}$.

We checked the validity of our approach by selecting a region within our data set at a time where the background and the plume+background were clearly identifiable, and we worked with the background and the residual (background-subtracted) plume radiance to build separate $\epsilon(T_e)$ versus $T_e$ profiles for the background and for the plume. It turns out that the DEMs evaluated by the two methods agree within a few percent.

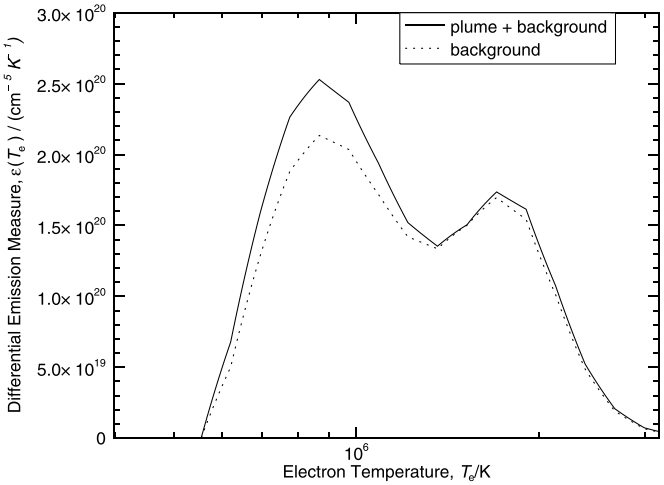


**Figure 8.** Differential emission measure, $\epsilon(T_e)$, versus Electron Temperature, $T_e$, over the time interval from 19:58 UTC to 20:08 UTC on 2010 August 28, from the 94 Å, 131 Å, 171 Å, 193 Å, 211 Å, and 335 Å channels. The solid line gives the $\epsilon(T_e)$ of the LOS-integrated emission along the axis of the plume (i.e., it is the plume+background $\epsilon(T_e)$) at a solar $y = 1003''$. The dotted line gives the $\epsilon(T_e)$ profile in a region devoid of plumes (i.e., it is the background $\epsilon(T_e)$) at the same solar $y$. The emission measure of the plume+background and of the background plasma can be evaluated by integrating $\epsilon(T_e)$ over d$T$ and turn out to be, respectively, $3.0 \times 10^{26}$ cm$^{-5}$ and $2.7 \times 10^{26}$ cm$^{-5}$.

Figure 8 also shows that the background $\epsilon(T_e)$ profile is composed of two components, respectively, peaking at $T_e$ values of $0.9 \times 10^6$ K and $1.8 \times 10^6$ K. Taking into account the widths of the two distributions (assumed to be Gaussians centered at the peak values of $T_e$/K), it turns out that the background corona is at an average temperature of $1.2 \times 10^6$ K, a value on the high side of the coronal electron temperatures listed by Wilhelm et al. (2011). From the residual plume emission, we analogously infer an average plume temperature of $8.5 \times 10^5$ K, consistent with plume temperatures given by Wilhelm et al. (2011). It is beyond the scope of this paper to discuss in detail the coronal temperatures. We do, however, remark that the value we obtained refers to an area within a small CH (possibly affected by the projection of high structures) where local differences between background regions are apparent: it is obvious from the images in Figure 1 that the radiance of the background corona on either side of the plume is not the same.

In Figure 9, we show the evolution with solar $y$, along the axis of the plume, of the plume $\epsilon(T_e)$ versus $T_e$ profiles (obtained from the difference between the plume+background and the background $\epsilon(T_e)$ curves, as described above), over the height range from solar-$y = 979''$ to solar-$y = 1015''$, at 08:40 and 19:58 UTC on August 28, that represent the initial and peak stage in the plume evolution. Data have been accumulated over 10 minutes; the figure gives profiles at four values of solar $y$ ($979''$, $991''$, $1003''$, and $1015''$). This shows that the highest values in the $\epsilon(T_e)$ versus $T_e$ profiles occur at $\approx T_e = (6$ to $8) \times 10^5$ K, possibly with a small shift toward lower temperatures with increasing solar $y$. The slight asymmetry in the profiles of the $\epsilon(T_e)$ versus $T_e$ plots may be due to a partially unsuccessful removal of the background, with its contribution having not been fully subtracted from the plume emission; however, we cannot rule out the possibility of a tiny amount of plasma at high temperature within the plume. The plume plasma, while not being strictly isothermal, changes its temperature by only a factor of $\leqslant$1.5 within the plume at each solar $y$. For instance, if we approximate with a Gaussian the profile at solar $y = 1003''$

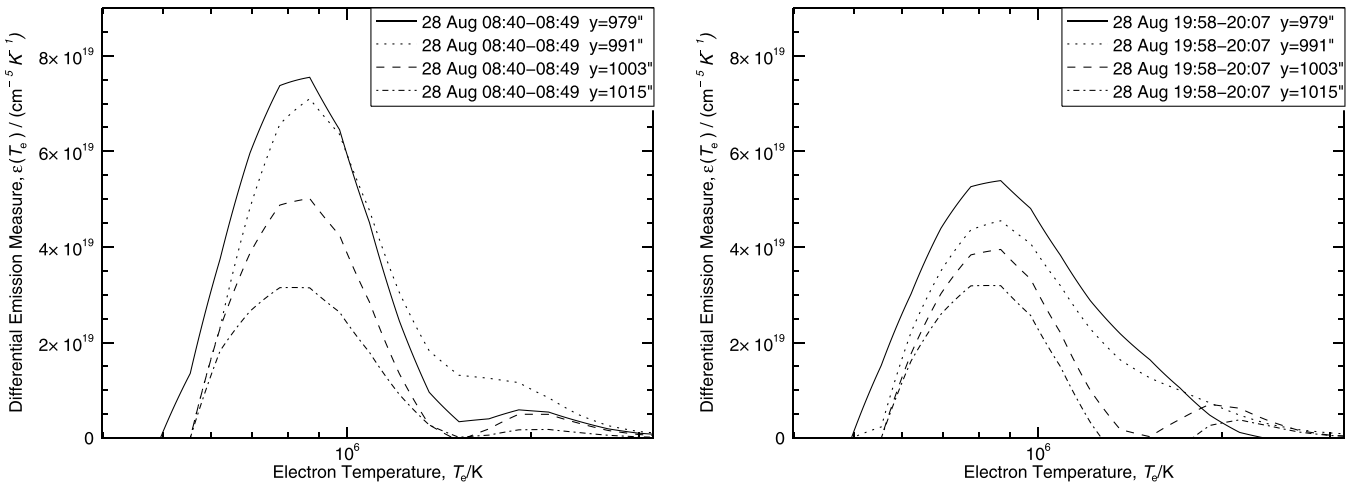


**Figure 9.** Differential emission measure, $\epsilon(T_e)$, versus electron temperature, $T_e$, at solar $y = 979''$, $991''$, $1003''$, and $1015''$, along the axis of the plume (respectively, solid, dotted, dashed, and dot-dashed lines) at two representative times of the plume's life. Left panel: profile at 08:40 UTC on 2010 August 28, during the initial stage of the plume's life. Right panel: profile at 19:58 UTC on 28 August, during the brightest stage of the plume's life. The background $\epsilon(T_e)$ profile has been subtracted from the plume+background $\epsilon(T_e)$ profile before plotting the plume $\epsilon(T_e)$ profile.

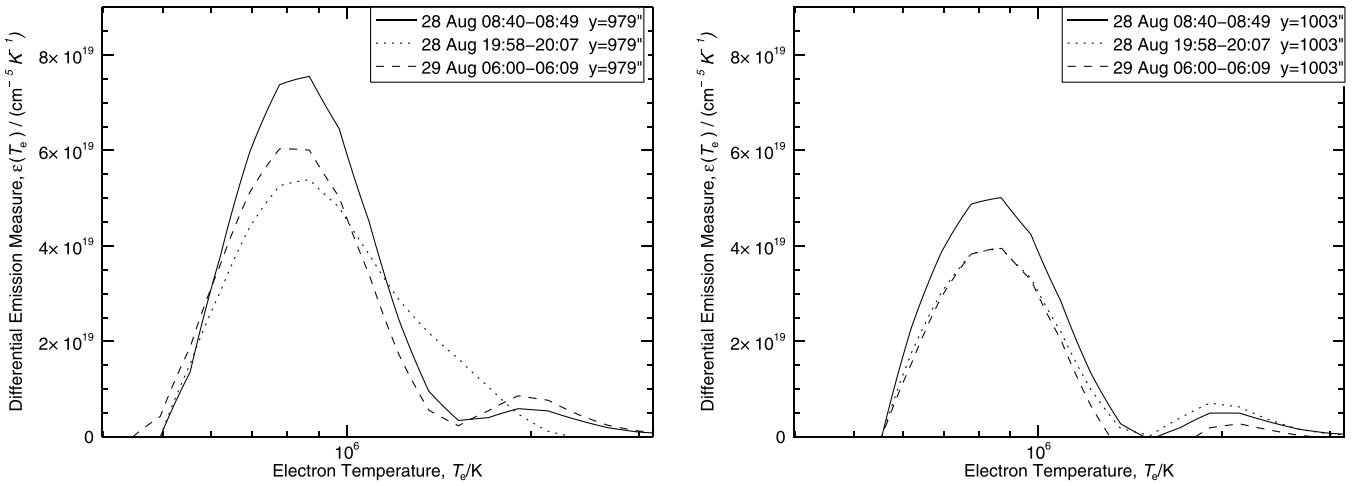


**Figure 10.** Time evolution of differential emission measure, $\epsilon(T_e)$, versus electron temperature, $T_e$, along the axis of the plume, after subtracting the background $\epsilon(T_e)$. Left: at solar $y = 979''$, at the initial (solid line), peak (dashed line), and final (dotted line) stage of the life of the plume. Right: same as left, but at solar $y = 1003''$.

**Table 1**
Density of the Plume Plasma

| Solar-$y$/″ | 979 | 991 | 1003 | 1015 |
|---|---|---|---|---|
| Time (UTC) | Plume electron density, $n_e$/cm$^{-3}$ | | | |
| Aug 28 08:40 | $3.1 \times 10^8$ | $3.2 \times 10^8$ | $2.4 \times 10^8$ | $1.9 \times 10^8$ |
| Aug 28 19:58 | $1.8 \times 10^8$ | $1.7 \times 10^8$ | $1.4 \times 10^8$ | $1.1 \times 10^8$ |
| Aug 29 06:00 | $1.7 \times 10^8$ | $1.3 \times 10^8$ | $1.1 \times 10^8$ | $9.3 \times 10^7$ |
| Time (UTC) | Background electron density, $n_e$/cm$^{-3}$ | | | |
| Aug 28 08:40 | $1.1 \times 10^8$ | $1.0 \times 10^8$ | $9.2 \times 10^7$ | $8.3 \times 10^7$ |
| Aug 28 19:58 | $1.1 \times 10^8$ | $9.8 \times 10^7$ | $8.8 \times 10^7$ | $8.0 \times 10^7$ |
| Aug 29 06:00 | $1.1 \times 10^8$ | $9.9 \times 10^7$ | $8.9 \times 10^7$ | $8.1 \times 10^7$ |

(dashed curve in the left panel of Figure 9), we evaluate that ≈68% of the plasma has temperatures between $6.5 \times 10^5$ K $\leqslant T_e \leqslant 1.1 \times 10^6$ K. Densities calculated from EMs (see Table 1), taking into account the increasing width versus solar $y$ of the plume, turn out to decrease over a solar-$y$ interval of ≈40″ by ≈50%–60%, independent of time. These densities decrease with time over the life of the plume by an amount that changes with solar $y$, ranging from a factor of about 60% at the lower solar $y$ (979″and 991″), to about a factor of two at the highest solar $y$ (1015″) that we sample. Over the entire lifetime of the plume, its density is highest at its birth.

Figure 10 gives the $\epsilon(T_e)$ versus $T_e$ profiles at solar $y = 979''$ and $1003''$ along the plume's axis, at times representative of the initial (08:40 UTC, August 28), peak (19:58 UTC, 28 August), and decay (06:00 UTC, August 29) phase of the plume. Data have been accumulated over 10 minutes starting at these times, and all AIA channels listed in Section 2, with the exception of the 304 Å channel, have been used.

Table 1 shows a resume of our results: densities at different heights and times in the plume are compared with the ambient coronal densities at the same altitude and same time. In order to estimate densities in the background corona, we assumed an LOS length of 0.5 solar radii.

## 5. DISCUSSION AND CONCLUSIONS

We have examined the behavior of a plume at several stages over its lifetime with the aim of clarifying its time evolution. In this section, we discuss separately the results we obtained for the three main areas we examined: the BP–plume relationship, outflows, and plume physical parameters.

### 5.1. The BP–Plume Relationship

The plume is rooted in a polar BP; the plume appears just after the BP appears and disappears shortly after the BP disappears.

Del Zanna et al. (2003) suggested that for at least some cases, plumes have BPs at their bases only during the early stages of the plumes' lives. Our observations for this plume instead show the plume to have a BP at its base for essentially the entirety of the plume's life. Here, we have examined only one case, and thus we cannot draw general conclusions. We do emphasize, however, that long-lasting data are required to define the characteristics of the BP–plume association. In our case, we agree with Del Zanna et al. (2003) in that BPs may be a prerequisite of plumes, but we cannot say that the association holds only in the first stages of the plume lifetime, because, in our case, the BP lives for nearly the entirety of the plume's life, with the BP starting two hours before the plume starts, and the plume fading one hour after the BP fades (see Figure 3).

Figure 2 shows that the plume is brightest early in its lifetime; as it evolves in time, the plume becomes fainter and wider, finally blending with the interplume medium. The temperature of the plume does not change with time, but its density decreases. Hence, the visibility of the plume depends crucially on its density. Over the plume's lifetime, the density changes by less than a factor of two at the lowest altitude. At higher altitudes, solar $y = 979''$ and above, the density decreases by $\approx$2, implying a decrease of at least a factor of four in plume XUV emission. Comparing the plume and background densities Table 1 shows that, early in the plume's life, densities along the plume's axis are about a factor of three higher than those of the ambient corona at solar $y = 979''$and $991''$, and a factor 2.5 higher than those of the ambient corona at solar $y = 1003''$and $1015''$. Late in the plume's life, the densities reduce to being only 50% higher than the background at the base and only 10% higher than the background at high altitudes.

This decrease over time may affect also the observability of plumes in the interplanetary medium. The issue of the plume survival at large heliocentric distances has been debated for years, but the identification of plumes with distant solar wind structures, such as pressure balanced structures (McComas et al. 1996; Poletto et al. 1996) or microstreams (Neugebauer 2012), has not yet been universally accepted. If our observations show behavior typical of all plumes, then plumes have a high density only over a limited fraction of their lifetime, and thus detection of a specific plume at interplanetary distances may be easier (or less difficult) only over a portion of that plume's life.

According to Wang (1998), plumes acquire high densities as a consequence of the evaporation of material triggered by reconnection-induced energy deposition, and eventually decay by radiative cooling. Assuming, as in Wang (1998), an evaporation time of $\tau_{ev} \approx L/u$, where $L$ is a vertical dimension and $u$ is characteristic flow speed, the formation of the plume a couple of hours after the BP implies that $u \approx 6\,\mathrm{km\,s^{-1}}$, which seems acceptable. The radiative cooling time, $\tau_{\rm rad}$, is given by $\tau_{\rm rad} \approx 3p/(2n^2\Lambda)$, where $\Lambda$ is the radiative loss function and $p$ is the plasma pressure; for $T_{\rm e} \approx 10^6$ K, $\Lambda \approx 10^{-22}$g s$^{-3}$ cm$^5$ (Priest 1984). Assuming $n \approx 3.1 \times 10^8$ cm$^{-3}$, it turns out that $\tau_{\rm rad} \approx 3$ hours, which is a little longer than the time-lag between the disappearance of the BP and the time when the plume blends with the background (see Figure 3). We don't know the reason for this discrepancy, but we point out that the lifetime of the BP might be longer, in case the fraction of its area behind the limb survives its visible side component, though at a very low radiance level.

Why does the plume fluctuate independently of the BP fluctuations? A possibility is that the BP brightens in response to reconnection episodes at its magnetic base. Looking at Figure 1, panels B and C, the many loops that show up in different locations seem to indicate that the BP base field could be made up of a number of magnetic fragments of each polarity that, later on, emerge, converge, and annihilate, eventually leading to the (loops and) BP disappearance (Von Rekowski & Hood 2008). The plume, on the other hand, likely originates from reconnection between the BP and the ambient unipolar field, and this process is not necessarily related to the process leading to the BP's fluctuations.

### 5.2. Outflows in Plumes and Background Regions

As mentioned in Section 3, the outflow speed of disturbances seen in the space–time maps has often been compared with the sound speed, to check whether the observed events might be interpreted as signatures of magneto-acoustic upward propagating waves. Such waves would be expected to induce spectral-line radiance oscillations traveling with a speed equal to or lower than the sound speed (Edwin & Roberts 1983). Recently, Krishna Prasad et al. (2011) and Gupta et al. (2012), on the basis of, respectively, AIA and SUMER data, present evidence supporting this scenario. Because Gupta et al. (2012) used data in the 171 Å and 193 Å AIA channels, their results are more easily compared with our work. These authors conclude that the characteristics of the observed events comply with the wave requirements, as the observed ratio of the propagating speed of the disturbances in the 171 Å and 193 Å channels is close enough to its theoretically expected value (1.19 in their observations compared to 1.25 in the theory). If we take into account the temperature of maximum emission in CHs and quiet Sun (which should be representative enough of the plume conditions) given by O'Dwyer et al. (2010) for the 171 Å and 193 Å channels, the expected theoretical ratio may be a little higher. However, Gupta et al. (2012) warn the reader that the alternative upflowing events scenario cannot be ruled out unless coordinated observations (combining imaging and spectroscopic data) become available.

In our analysis, the magnetoacoustic wave hypothesis is not tenable, because the 171 Å perturbations have a higher propagation speed than the 193 Å events. The reason for this discrepancy is not clear. It may originate from the fainter jets, which were not included in the analysis of Gupta et al. (2012), but which in our work are the jets with higher propagation speeds. Hence, we are led to favor the interpretation of McIntosh et al. (2010) and Tian et al. (2011) who from *STEREO* and AIA data, respectively, conclude that the observed disturbances represent high-speed outflows.

Tian et al. (2011) do not give the outflow speed distributions in different AIA channels, and the distribution they show peaks at a somewhat lower value ($\approx$130 km s$^{-1}$ vs. 167 km s$^{-1}$) than our 171 Å distribution (see Figure 6). If we consider events in all AIA channels, we get a mean speed of 150 km s$^{-1}$, in good agreement with Tian et al. (2011), being within the Gaussian width (30 km s$^{-1}$) of their distribution. We should also consider that the upward speed may show some variability, depending on the individual data set being analyzed. We point out that the occurrence rate and the speed distribution of propagating disturbances do not depend on the age of our plume, as both remain about constant as the plume approaches the time of its disappearance (see Figure 7).

An interesting issue that has also been mentioned, though briefly, by Tian et al. (2011), is the occurrence of upflowing

events in the background interplume corona. Figure 6 (bottom row) gives our measurements of the speed distribution of the 171 Å and 193 Å upflow events in the background corona. A comparison of this with the top row of analogous plume distributions of Figure 6 reveals that, apart from a lower number of events, there is no major difference between the plume and interplume distributions of the 193 Å channel while in the 171 Å channel the peak value of the background corona outflow speed distribution is somewhat lower. Furthermore, both distributions (plume and interplume) do not show any temperature dependence of the outflow speed. Because the background ambient corona has a lower density than the plume, we do not know whether the interplume regions host fewer events, or whether their detection is more difficult due to their lower-density environment. A detailed analysis of this problem is beyond the aim of this presentation. However, if future studies substantiate that upflows occur in the ambient corona, the implications for those upflows as solar wind sources, and their implications for plume-versus-interplume contributions to the solar wind, should be reconsidered. Solar minimum conditions, when the occurrence of bright features along the Sun–Earth LOS is minimized, are a better fit for these types of investigations.

We cannot say from our data whether the observed events reach high heliocentric distances and feed the solar wind. If we assume that they do, we may give an upper estimate of the mass contributed by the disturbances to the wind. We will assume plumes covering some 10% of a typical polar CH extending down to a 70° latitude; this percentage occupation (Ahmad & Withbroe 1977) is probably an upper limit to the actual coverage of plumes. If upflows rise from the whole plume area—a further unknown factor—with a characteristic speed of 100 km $s^{-1}$ and a density of $10^8$ $cm^{-3}$, it turns out that about 60% of the wind mass may originate from plumes within one polar CH. However, not knowing how much of the plume area is outflowing, nor out to what distance from the Sun the outflows persist and if plasma accelerates enough to escape from the Sun, this figure may be easily affected by one order of magnitude uncertainty (or even more, should outflows die within a short distance from the limb). We point out that the work of Llebaria et al. (2002), where plume trajectories and plume speeds have been followed over time intervals of the order of hours and out to heliocentric distances of the order of a few solar radii, suggest that plume outflows may actually contribute substantially to the solar wind.

A further factor that might be used to understand whether plumes contribute to solar wind, is the comparison of their first ionization potential (FIP) bias with that measured in fast wind (Von Steiger et al. 2000). According to some workers (Widing & Feldman 1992; Wilhelm & Bodmer 1998; Curdt et al. 2008), the FIP bias in plumes differs enough from that of the fast wind to rule plumes out as fast-wind contributers. However, it is fair to say that the issue is not completely settled, as Del Zanna et al. (2003) claim, there is no significant fractionation in plumes. Because our data are not fit for an abundance analysis, we do not deal any further with this issue.

### 5.3. Physical Parameters of Plumes

The values of densities given in Table 1 and the temperatures that we quote in Section 4 are more or less consistent with the values inferred by other authors. Possibly, the slightly higher value of the ambient coronal temperature in our analysis results from data being acquired inside a small hole, when the LOS is likely affected by features along the LOS-integration path. What is worth noting, however, is that our inferred plume temperatures remain approximately unchanged over the lifetime of the plume, as this implies that plumes die due to a density reduction over time, at least for the single plume examined here.

This result, together with the observed lack of change with time in the occurrence of outflows, may lead to a scenario where plumes—at least those associated with BPs—are sort of a "bush" residing above a base that is powered by reconnection episodes; those episodes would be triggered more frequently by the BP magnetic fields than elsewhere. The reconnections would lead to high-density plasma evaporation, making plumes denser and more visible than the surrounding ambient corona. Under this scenario, the outflows we observe as low-level radiance enhancements may represent the outcome of reconnections that are relatively energetic compared to the comparatively gentle magnetic events occurring in nearby surrounding areas of the CH, resulting in the plumes standing out in the ambient CH corona. As long as the BP magnetic field does not disperse or annihilate, reconnection events continue to occur. The 193 Å and 211 Å panels of Figure 1 (panels B, C, E, F, H, and I) suggest that the compact loops that are observed early in the lifetime of the BP tend to grow fainter, and possibly wider, as time goes by. This may indicate that the BP base fields become more sparse: over time, we are likely lead to more sparse evaporating episodes and, hence, to a decrease in the overall plume's density and, eventually, to the plume death as the BP base fields fade and become indistinguishable from the coronal background ambient fields. We surmise that individual evaporating episodes may keep occurring throughout the plume lifetime, but their numbers decrease with time, until they become as few and weak as we observe in the background corona.

S.P. and G.P. acknowledge support from ASI I/023/09/0. A.C.S. was supported by funding from NASA's Office of Space Science through the Living With a Star Targeted Research & Technology Program. A.C.S. also benefited from discussions held at the International Space Science Institute's (ISSI, Bern, Switzerland) International Team on Solar Coronal Jets.

## REFERENCES

Ahmad, I. A., & Withbroe, G. L. 1977, SoPh, 53, 397
Boerner, P. F., Testa, P., Warren, H., Weber, M. A., & Schrijver, C. J. 2014, SoPh, 289, 2377
Chandrashekhar, K., Krishna Prasad, S., Banerjee, D., Ravindra, B., & Seaton, D. B. 2013, SoPh, 286, 125
Curdt, W., Wilhelm, K., Feng, L., & Kamio, S. 2008, A&A, 481, L61
Del Zanna, G., Bromage, B. J. I., & Mason, H. E. 2003, A&A, 398, 743
Edwin, P. M., & Roberts, B. 1983, SoPh, 88, 179
Gabriel, A. H., Bely-Dubau, F., & Lemaire, P. 2003, ApJ, 589, 623
Gupta, G. R., Teriaca, L., Marsch, E., Solanki, S. K., & Banerjee, D 2012, A&A, 546, A93
Kariyappa, R., & Varghese, B. A. 2008, A&A, 485, 289
Krishna Prasad, S., Banerjee, D., & Gupta, G. R. 2011, A&A, 528, L4
Lemen, J. R., Title, A. M., Akin, D. J., et al. 2012, SoPh, 275, 17
Llebaria, A., Saez, F., & Lamy, P. 2002, in Proc. SOHO 11 Symposium on From Solar Min to Max: Half a Solar Cycle with SOHO, ed. A. Wilson (ESA-SP 508; Noordwijk: ESA), 391
McComas, D. J., Hogeeveen, G. W., Gosling, J. T., Phillips, J. L., et al. 1996, A&A, 316, 368
McIntosh, S. W., Innes, D. E., De Pontieu, B., & Leamon, R. J. 2010, A&A, 510, L2
Neugebauer, M. 2012, ApJ, 750, 50
Noci, G., Kohl, J. L., & Withbroe, G. L. 1987, ApJ, 315, 706
O'Dwyer, B., Del Zanna, G., Mason, H. E., Weber, M. A., & Tripathi, D. 2010, A&A, 521, A21
Pesnell, W. D., Thompson, B. J., & Chamberlin, P. C. 2012, SoPh, 275, 3
Plowman, J., Kankelborg, C., & Martens, P. 2013, ApJ, 771, 2
Poletto, G., Parenti, S., Noci, G., Livi, S., et al. 1996, A&A, 316, 374

Priest, E. R. 1984, in Solar Magnetohydrodynamics (Dordrecht: Reidel)
Raouafi, N.-E., Petrie, G. J. D., Norton, A. A., et al. 2008, ApJL, 682, L137
Teriaca, L, Poletto, G., Romoli, M., & Biesecker, D. A. 2003, ApJ, 588, 566
Tian, H., McIntosh, S. W., Habbal, S. R., & He, J. 2011, ApJ, 736, 130
Tian, H., Tu, C., Marsch, E., He, J., & Kamio, S. 2010, ApJL, 709, L88
von Rekowski, B., & Hood, A. W. 2008, MNRAS, 384, 972
von Steiger, R., Schwadron, N. A., Fisk, L. A., Geiss, J., et al. 2000, JGR, 105, 27217
Wang, Y.-M. 1998, ApJL, 501, L145
Wang, Y.-M., & Muglach, K. 2008, SoPh, 249, 17
Widing, K. G., & Feldman, U. 1992, ApJ, 392, 715
Wilhelm, K., Abbo, L., Auchère, F., et al. 2011, A&ARv, 19, 35
Wilhelm, K., & Bodmer, R. 1998, SSRv, 85, 371
Wilhelm, K., Dammasch, I. E., Marsch, E., & Hassler, D. M. 2000, A&A, 353, 749
Zhang, Q. M., Chen, P. F., Guo, Y., et al. 2012, ApJ, 746, 19